

Ceci n'est pas a globular cluster: the metallicity distribution of the stellar system Terzan 5 ¹

D. Massari², A. Mucciarelli², F. R. Ferraro², L. Origlia³, R. M. Rich⁴, B. Lanzoni², E. Dalessandro², E. Valenti⁵, R. Ibata⁶, L. Lovisi², M. Bellazzini³, D. Reitzel⁴

² *Dipartimento di Fisica e Astronomia, Università degli Studi di Bologna, v.le Berti Pichat 6/2, I-40127 Bologna, Italy*

³ *INAF-Osservatorio Astronomico di Bologna, via Ranzani 1, 40127, Bologna, Italy*

⁴ *Department of Physics and Astronomy, Math-Sciences 8979, UCLA, Los Angeles, CA 90095-1562, USA*

⁵ *European Southern Observatory, Karl-Schwarzschild-Strasse 2, 85748 Garching bei München, Germany*

⁶ *Observatoire Astronomique, Université de Strasbourg, CNRS, 11, rue de l'Université. F-67000 Strasbourg, France*

30 Jul, 2014

ABSTRACT

We present new determinations of the iron abundance for 220 stars belonging to the stellar system Terzan 5 in the Galactic bulge. The spectra have been acquired with FLAMES at the Very Large Telescope of the European Southern Observatory and DEIMOS at the Keck II Telescope. This is by far the largest spectroscopic sample of stars ever observed in this stellar system. From this dataset, a subsample of targets with spectra unaffected by TiO bands was extracted and statistically decontaminated from field stars. Once combined with 34 additional stars previously published by our group, a total sample of 135 member stars covering the entire radial extent of the system has been used to determine the metallicity distribution function of Terzan 5. The iron distribution clearly shows three peaks: a super-solar component at $[\text{Fe}/\text{H}] \simeq 0.25$ dex, accounting for $\sim 29\%$ of the sample, a dominant sub-solar population at $[\text{Fe}/\text{H}] \simeq -0.30$ dex, corresponding to $\sim 62\%$ of the total, and a minor (6%) metal-poor component at $[\text{Fe}/\text{H}] \simeq -0.8$ dex. Such a broad, multi-modal metallicity distribution demonstrates that Terzan 5 is not a genuine globular cluster but the remnant of a much more complex stellar system.

Subject headings: stellar system: individual (Terzan 5); stars: abundances; techniques: spectroscopic

1. INTRODUCTION

Terzan 5 is a stellar system located in the bulge of our Galaxy, at a distance of 5.9 kpc (Valenti et al. 2007), historically classified as a globular cluster (GC). Its location ($l = 3.8395^\circ$, $b = 1.6868^\circ$) corresponds to a highly extinguished region of the sky, with an average color excess $E(B - V) = 2.38$ mag (Valenti et al. 2007) and a patchy structure of dust clouds that causes the extinction to vary spatially by ~ 0.7 mag over a projected spatial scale of few arcminutes (Massari et al. 2012). Because of optical observations of Terzan 5 are extremely challenging, its true nature remained hidden behind this dusty curtain for a long time, until high-resolution near-infrared observations revealed the presence of two distinct stellar populations (Ferraro et al. 2009, hereafter F09). Two Red Clumps (RCs) well separated in color ($\delta(J-K) \sim 0.2$ mag) and magnitude ($\Delta K \sim 0.3$ mag) have been detected in the near-infrared color magnitude diagram (CMD) obtained with the Multi-conjugate Adaptive optics Demonstrator (MAD) mounted at the Very Large Telescope. The analysis of near-infrared high-resolution spectra (Origlia et al. 1997) promptly acquired with NIRSPEC (McLean et al. 1998) at Keck II telescope demonstrated that both populations belong to Terzan 5 and have very different iron abundances (F09; Origlia et al. 2011, hereafter O11): $[Fe/H] = -0.25$ dex for the component corresponding to the faint RC, $[Fe/H] = +0.27$ dex for the bright RC. Recently, Origlia et al. (2013, hereafter O13) discovered the presence of a third, more metal-poor component at $[Fe/H] = -0.79$. Such a large spread in the iron abundance of Terzan 5 stars clearly indicates that its initial mass had to be much larger than the current one ($10^6 M_\odot$, Lanzoni et al. 2010), in order to retain the high-velocity, iron-enriched gas ejected by supernovae (SN). Moreover, O11 did not find any hint of the spreads and anti-correlations among light elements commonly observed in Galactic GCs (see Carretta et al. 2010a). Instead, the α -element abundance patterns of the three populations (see O11, O13) turned out to be strikingly similar to those observed in the bulge field stars (e.g., Fulbright et al. 2007; Hill et al. 2011; Rich et al. 2012; Johnson et al. 2011, 2012, 2013,

¹Based on FLAMES observations performed at the European Southern Observatory, proposal numbers 087.D-0716(B), 087.D-0748(A) and 283.D-5027(A), and at the W. M. Keck Observatory. Keck is operated as a scientific partnership among the California Institute of Technology, the University of California, and the National Aeronautics and Space Administration. The Observatory was made possible by the generous financial support of the W. M. Keck Foundation.

2014; Ness et al. 2013), with α -enhancement up to about solar $[\text{Fe}/\text{H}]$ and a progressively decreasing $[\alpha/\text{Fe}]$ towards the solar ratio at super-solar $[\text{Fe}/\text{H}]$.

The observational evidence collected so far suggests that Terzan 5 is not a genuine GC, but a stellar system that experienced complex star formation and chemical enrichment histories. In order to accurately reconstruct its evolution, a first crucial step is to precisely determine the metallicity distribution of its stellar populations, based on a statistically significant sample of stars. This paper reports the iron abundance for a sample of 220 giants distributed over the entire radial extent of Terzan 5, from the innermost regions, out to the tidal radius. In Section 2 we present the analyzed sample. In Section 3 we describe the chemical abundance analysis. The overall error budget is discussed in Section 4. Finally in Section 5 we finally present the metallicity distribution and in Section 6 we draw our conclusions.

2. OBSERVATIONS AND DATA REDUCTION

This work is part of a large spectroscopic survey of stars in the direction of Terzan 5, aimed at characterizing the kinematical and chemical properties of the stellar populations within the system and in the surrounding Galactic bulge field. While the overall survey will be described in a forthcoming paper (Ferraro et al. 2014 in preparation) and the properties of the field around Terzan 5 have been discussed in Massari et al. (2014, hereafter M14a), here we focus on the metallicity distribution of Terzan 5.

This study is based on a sample of stars located within the tidal radius of Terzan 5 ($r_t \simeq 300''$; Lanzoni et al. 2010; Mocchi et al. 2013) observed with two different instruments: FLAMES (Pasquini et al. 2002) at the ESO Very Large Telescope (VLT) and DEIMOS (Faber et al. 2003) at the Keck II Telescope. The spectroscopic targets have been selected from the optical photometric catalog of Terzan 5 described in Lanzoni et al. (2010) along the brightest portion ($I < 17$) of the red giant branch (RGB). In order to avoid contamination from other sources, in the selection process of the spectroscopic targets we avoided stars with bright neighbors ($I_{neighbor} < I_{star} + 1.0$) within a distance of $2''$. The spatial distribution of the observed targets is shown in Fig. 1.

(1) *FLAMES dataset*— This dataset has been collected under three different programs (ID: 087.D-0716(B), PI: Ferraro, ID: 087.D-0748(A), PI: Lovisi and ID: 283.D-5027(A), PI: Ferraro). As already described in M14a, all the spectra have been obtained using the HR21 setup in the GIRAFFE/MEDUSA mode, providing a resolving power of $R \sim 16200$ and a spectral coverage ranging from 8484 Å to 9001 Å. This grating has been chosen because it

includes the prominent Ca II triplet lines, which are widely used features for radial velocity estimates, even in low signal-to-noise ratio (SNR) spectra. Several metal lines (mainly of Fe I) lie in this spectral range, thus allowing a direct measurement of [Fe/H]. In order to reach SNR \sim 40-50 even for the faintest ($I \sim 17$) targets, multiple exposures with integration times ranging from 1500 s to 2400 s (depending on the magnitude of the targets) have been secured for the majority of the stars. In order to reduce the acquired spectra we used the FLAMES-GIRAFFE ESO pipeline². This includes bias-subtraction, flat-field correction, wavelength calibration with a standard Th-Ar lamp, resampling at a constant pixel-size and extraction of one-dimensional spectra. Because of the large number of O₂ and OH emission lines in this spectral range, a correct sky subtraction is a primary requirement. Thus, in each exposure 15-20 fibers have been used to measure the sky. The master sky spectrum obtained as the median of these spectra has been then subtracted from the stellar ones. Finally, all the spectra have been reported to zero-velocity and in the case of multiple exposures they have been co-added together.

(2) *DEIMOS dataset*— This spectral dataset has been acquired by using the 1200 line/mm grating coupled with the GG495 and GG550 order-blocking filters. The spectra cover the \sim 6500-9500 Å wavelength range with a resolution of $R \sim 7000$ at $\lambda \sim 8500$ Å. An exposure time of 600 s for each pointing allowed to reach SNR \sim 50 – 60 for the brightest stars and SNR \sim 15 – 20 for the faintest ones ($I \sim 17$ mag). We used the package described in Ibata et al. (2011) for an optimal reduction and extraction of the DEIMOS spectra.

For sake of comparison, Fig. 2 shows two spectra of the same star observed with FLAMES (top panels) and with DEIMOS (bottom panels).

3. ANALYSIS

3.1. Atmospheric parameters

Effective temperatures (T_{eff}) and surface gravities ($\log g$) for each target have been derived from near infrared photometry in order to minimize the effect of possible residuals in the differential reddening correction. The ($K, J - K$) CMD has been obtained by combining the SOFI catalog of Valenti et al. (2007) for the central $2.5' \times 2.5'$ and 2MASS photometry in the outermost regions. Magnitudes and colors of each star have been corrected for differential extinction according to their spatial location with respect to the center of Terzan 5. For stars in the innermost regions, lying within the field of view (FoV) of the ACS/HST observations

²<http://www.eso.org/sci/software/pipelines/>

(see Lanzoni et al. 2010), the reddening map published in Massari et al. (2012)³ has been adopted. Instead the correction for stars in the outer regions has been estimated from the new differential reddening map described in M14a (see their Figure 4). The target positions in the reddening-corrected CMD are shown in Fig. 3. In order to estimate T_{eff} and $\log g$, the position of each target in the reddening-corrected CMD has been projected onto a reference isochrone. Following F09, we adopted a 12 Gyr-old isochrone extracted from the BaSTI database (Pietrinferni et al. 2006) with metallicity $Z=0.01$ (corresponding to $[\text{Fe}/\text{H}]=-0.25$), α -enhanced chemical mixture and helium content $Y=0.26$ dex (well reproducing the dominant stellar population in Terzan 5, see O11). The isochrone is shown as dashed line in Fig. 3. Since Terzan 5 hosts at least two stellar populations, but they are photometrically indistinguishable in the near-infrared plane, in Section 4, we discuss the effect of using isochrones with different metallicities and ages.

As already explained in M14a, the small number (about 10) of Fe I lines observed in the FLAMES and DEIMOS spectra (see Section 3.2) prevents us from deriving a reliable spectroscopic determination of the microturbulent velocity (v_{turb} ; see Mucciarelli 2011 for a review of the different methods to estimate this parameter). Therefore, for homogeneity with our previous work we adopted the same value, $v_{\text{turb}}=1.5 \text{ km s}^{-1}$, which is a reasonable assumption for cool giant stars (see also Zoccali et al. 2008; Johnson et al. 2013).

3.2. Chemical analysis

We adopted the same Fe I linelist and the same techniques to analyze the spectra and to determine the chemical abundances as those used in M14a.

(1) *FLAMES data-set*— We performed the chemical analysis using the package GALA (Mucciarelli et al. 2013)⁴, an automatic tool to derive chemical abundances of single, unblended lines by using their measured equivalent widths (EWs). The adopted model atmospheres have been calculated with the ATLAS9 code (Castelli & Kurucz 2004). Following the prescriptions by M14a, we performed the analysis running GALA with all the model atmosphere parameters fixed and allowing only the metallicity to vary iteratively in order to match the iron abundance measured from EWs. The latter were measured by using the

³A webtool able to compute the reddening in the direction of Terzan 5 is freely available at the Cosmic-lab website, <http://www.cosmic-lab.eu/Cosmic-Lab/Products.html>

⁴GALA is freely distributed at the Cosmic-Lab project website, <http://www.cosmic-lab.eu/gala/gala.php>

code 4DAO (Mucciarelli 2013)⁵. This code runs DAOSPEC (Stetson & Pancino 2008) for large sets of spectra, tuning automatically the main input parameters used by DAOSPEC. It also provides graphical outputs that are fundamental to visually check the quality of the fit for each individual spectral line. EW errors are estimated by DAOSPEC as the standard deviation of the local flux residuals (see Stetson & Pancino 2008). All the lines with EW errors larger than 10% were excluded from the analysis.

(2) *DEIMOS data-set*— The lower resolution of DEIMOS causes a high degree of line blending and blanketing in the observed spectra. The derivation of the abundances through the method of the EWs is therefore quite uncertain. Thus, the iron abundances for this dataset have been measured by comparing the observed spectra with a grid of synthetic spectra, according to the procedure described in Mucciarelli et al. (2012). Each Fe I line has been analyzed individually by performing a χ^2 -minimization between the normalized observed spectrum and a grid of synthetic spectra. The synthetic spectra have been computed with the code SYNTH (Sbordone et al. 2004) assuming the proper atmospheric parameters for each individual star, then convolved at the DEIMOS resolution and finally resampled at the pixel size of the observed spectra. To improve the quality of the fit, the normalization is iteratively readjusted locally in a region of ~ 50 -60 Å. We estimated the uncertainties in the fitting procedure for each spectral line by using Monte Carlo simulations: for each line, Poissonian noise is added to the best-fit synthetic spectrum in order to reproduce the observed SNR and then the fit is re-computed as described above. The dispersion of the abundance distribution derived from 1000 Monte Carlo realizations has been adopted as the abundance uncertainty (typically about ± 0.2 dex).

4. Error budget

In order to verify the robustness of our abundance analysis, in the following we discuss the effect of each specific assumption we made and the global uncertainty on the iron abundance estimates.

4.1. Systematic effects

1. *Choice of the isochrone.* The atmospheric parameters of the selected targets have been determined from the projection onto an isochrone corresponding to the old, sub-solar

⁵4DAO is freely distributed at the website <http://www.cosmic-lab.eu/4dao/4dao.php>.

population (see Fig.3). However, as discussed by F09 and O11, Terzan 5 hosts at least two stellar populations with different iron abundances and possibly ages. In order to quantify the effect of using isochrones with different metallicity/age, we re-derived the atmospheric parameters by using a BaSTI isochrone (Pietrinferni et al. 2004) with an age of 6 Gyr, $Z=+0.03$ and a solar-scaled mixture (corresponding to $[\text{Fe}/\text{H}]=+0.26$ dex). The temperatures of the targets decrease by less than 200 K and the gravities increase by ~ 0.2 (as a consequence of the larger evolutive mass). By re-analyzing the spectra of these stars with the new parameters, we obtained very similar iron abundances, the mean difference and rms scatter being $\langle [\text{Fe}/\text{H}]_{6 \text{ Gyr}} - [\text{Fe}/\text{H}]_{12 \text{ Gyr}} \rangle = 0.00$ dex and $\sigma = 0.12$ dex, respectively. We performed an additional check by adopting the metallicity of the extreme metal poor component ($[\text{Fe}/\text{H}] \simeq -0.8$ dex), by using a BaSTI isochrone with an age of 12 Gyr, $Z=0.004$ and α -enhanced (corresponding to $[\text{Fe}/\text{H}] \simeq -1$ dex), finding that iron abundances increase only by about 0.06 dex.

2. *Temperature scale.* To check the impact of different T_{eff} scales we derived the atmospheric parameters by adopting the Dartmouth (Dotter et al. 2007) and Padua (Marigo et al. 2008) isochrones, and we found negligible variations ($\delta T_{\text{eff}} \leq 50$ K). Also the adoption of the $(J - K) - T_{\text{eff}}$ empirical scale by Montegriffo et al. (1998) has a marginal impact (smaller than 100 K) on the derived temperatures. Such differences lead to iron variations smaller than 0.05 dex.
3. *Microturbulent velocities.* The assumption of a different value of v_{turb} has the effect of shifting the metallicity distribution, without changing its shape. Typically, a variation of $\pm 0.1 \text{ km s}^{-1}$ leads to iron abundance variations of $\mp 0.07 - 0.1$ dex. Given the typical dispersion of v_{turb} for this kind of stars (see M14a), this effect would lead to a systematic shift of the distribution of a few tenths of dex. However the nice match between the abundances measured in these work and those obtained by O11 and O13 from higher-resolution spectra for the targets in common (see Section 5.1) demonstrates that our choice of v_{turb} is adequate.
4. *Model atmospheres.* We repeated the analysis of the targets by adopting MARCS (Gustafsson et al. 2008) and ATLAS9-APOGEE (Mezсарos et al. 2012) model atmospheres, instead of the ATLAS9 models by Castelli & Kurucz (2004). The adoption of different model atmospheres calculated assuming different lists for opacity, atomic data and computation recipes leads to variations smaller than ± 0.1 dex in the $[\text{Fe}/\text{H}]$ determination, and it does not change the shape of the metallicity distribution.

4.2. Abundance uncertainties

As discussed in M14a, the global uncertainty of the derived iron abundances (typically ~ 0.2 dex) has been computed as the sum in quadrature of two different sources of error.

(i) The first one is the error arising from the uncertainties on the atmospheric parameters. Since they have been derived from photometry, the formal uncertainty on these quantities depends on all those parameters which can affect the location of the targets in the CMD, such as photometric errors (σ_K and σ_{J-K} for the magnitude and the color, respectively), uncertainty on the absolute and differential reddening ($\sigma_{[E(B-V)]}$ and $\sigma_{\delta[E(B-V)]}$, respectively) and errors on the distance modulus (σ_{DM}). In order to evaluate the uncertainties on T_{eff} and $\log g$ we therefore repeated the projection onto the isochrone for every single target assuming $\sigma_K = 0.04$, $\sigma_{J-K} = 0.05$, $\sigma_{\delta[E(B-V)]} = 0.05$ for the targets in the ACS sample (Massari et al. 2012), $\sigma_{\delta[E(B-V)]} = 0.1$ for targets in the WFI FoV (M14a), and $\sigma_{[E(B-V)]} = 0.05$ and $\sigma_{DM} = 0.05$ (Valenti et al. 2010). We found that uncertainties on T_{eff} range from ~ 60 K up to ~ 120 K, and those on $\log g$ are of the order of 0.1-0.15 dex. For v_{turb} we adopted a conservative uncertainty of 0.2 km s^{-1} .

(ii) The second source of error is the internal abundance uncertainty. For each target this was estimated as the dispersion of the abundances derived from the lines used, divided by the squared root of the number of lines. It is worth noticing that, for any given star, the dispersion is calculated by weighting the abundance of each line by its own uncertainty (as estimated by DAOSPEC for the FLAMES targets, and from Monte Carlo simulations for the DEIMOS targets).

5. RESULTS

5.1. Metallicity distribution

In order to build the metallicity distribution of Terzan 5, we selected bona fide members according to the following criteria:

(i) we considered only stars within the tidal radius of Terzan 5 ($\sim 4.6'$, Lanzoni et al. 2010, see also Miocchi et al. 2013);

(ii) we considered stars with radial velocities within $\pm 2.5\sigma$ (between -123 km s^{-1} and -43 km s^{-1}) around the systemic radial velocity of Terzan 5 ($v_{\text{rad}} \simeq -83 \text{ km s}^{-1}$, Ferraro et al. 2014 in preparation);

(iii) we discarded spectra affected by TiO molecular bands, which can make difficult the evaluation of the continuum level and in the most extreme cases they completely hide the spectral lines of interest. To evaluate the impact of TiO bands on the observed spectra we followed the strategy described in M14a, adopting the same q-parameter (defined as the ratio between the deepest feature of the TiO band at $\sim 8860 \text{ \AA}$ and the continuum level measured in the adjacent spectral range $8850 \text{ \AA} < \lambda < 8856 \text{ \AA}$). Thus we analyzed the full set of absorption lines in all the targets with $q > 0.8$, while we adopted a reduced linelist (by selecting only iron absorption lines in the range $8680 \text{ \AA} < \lambda < 8850 \text{ \AA}$, which are only marginally affected by TiO contamination) for stars with $0.6 < q < 0.8$, and we completely discarded all the targets with $q < 0.6$ (see the empty symbols in Figure 3).

Following these criteria, we selected a sample of 224 stars (170 from the FLAMES dataset and 54 from the DEIMOS dataset). A few stars observed with different instruments were used to check the internal consistency of the measures. In fact, three DEIMOS targets are in common with the FLAMES sample and the average difference between the metallicity estimates is $\langle [\text{Fe}/\text{H}]_{\text{DEIMOS}} - [\text{Fe}/\text{H}]_{\text{FLAMES}} \rangle = +0.07 \pm 0.06$ ($\sigma = 0.11$ dex). One DEIMOS target is in common with the NIRSPEC sample by O11 and we find $[\text{Fe}/\text{H}]_{\text{DEIMOS}} - [\text{Fe}/\text{H}]_{\text{NIRSPEC}} = +0.02$ dex. Finally, three metal-poor FLAMES stars have been observed at higher spectral resolution with NIRSPEC by O13, and the average difference between the iron abundance estimates is 0.01 ± 0.02 dex ($\sigma = 0.03$), only. Hence we can conclude that iron abundances obtained from different instruments are in good agreement (well within the errors). For those stars with multiple measurements we adopted the iron abundance obtained from the dataset observed at higher spectral resolution. Thus the selected sample numbers 220 stars.

As discussed in detail in M14a, the rejection of targets severely contaminated by TiO bands introduces a bias that leads to the systematic exclusion of metal-rich stars. To avoid such a bias, we will focus the analysis only on a sub-sample of stars selected in a magnitude range ($9.6 < K_c < 11.7$) where no targets have been discarded because of TiO contamination. Thus, the final sample discussed in the following contains a total of 135 stars and their measured iron abundances and final uncertainties (computed as described in Section 4.2), together with the adopted atmospheric parameters, are listed in Table 1. The $[\text{Fe}/\text{H}]$ distribution for these 135 targets is shown in Figure 4. It is quite broad, extending from $[\text{Fe}/\text{H}] = -1.01$ to $+0.94$ dex, with an average value of $[\text{Fe}/\text{H}] = -0.12$ and a dispersion $\sigma = 0.35$, much larger than the typical uncertainty on the abundance estimates. More in details, the observed distribution shows a main peak at $[\text{Fe}/\text{H}] \sim -0.30$ dex and a secondary component at $[\text{Fe}/\text{H}] \sim +0.30$ dex, in very good agreement with the results of O11. Also the third component discovered by O13 is clearly visible at $[\text{Fe}/\text{H}] \simeq -0.8$ dex. The distribution also shows a very metal-rich tail, up to $[\text{Fe}/\text{H}] \sim +0.8$ dex. However, only five stars have been measured with such an extreme metallicity value, with a somewhat larger uncertainty

(~ 0.2 dex). Figure 5 shows the spectra of two such super metal-rich stars (7009197 and 7036045 with metallicity of $[\text{Fe}/\text{H}] = +0.77$ dex and $[\text{Fe}/\text{H}] = +0.74$ dex, respectively), and the spectrum of a star with $[\text{Fe}/\text{H}] = +0.26$ dex and very similar atmospheric parameters ($T_{\text{eff}} = 4325\text{K}$, $\log g = 1.7$ dex for the two super metal-rich targets and $T_{\text{eff}} = 4269\text{K}$ and $\log g = 1.6$ dex for the latter). As can be seen, the super metal-rich stars have deeper iron absorption lines, thus indicating a higher metal content with respect to the star at $[\text{Fe}/\text{H}] = +0.26$ dex. Note that in order to fit these lines with an iron abundance of 0.3 dex, one needs to assume a significantly warmer (~ 500 K) temperature. A spectroscopic followup at higher spectral resolution is needed to draw a more firm conclusions about the metal content of these stars. If their extremely high metallicity were confirmed, they would be among the most metal-rich stars in the Galaxy.

5.2. Statistical decontamination

Even though our sample has been selected within the narrow radial velocity range around the systemic velocity of Terzan 5, we may expect some contamination by a few bulge field stars. Hence, we performed a statistical decontamination by using the properties of the field population surrounding Terzan 5 described in M14a. As shown in detail in that paper, we found that the bulge field population has a very broad radial velocity distribution, peaking at $v_{\text{rad,field}} \sim 21 \text{ km s}^{-1}$ and with a dispersion $\sigma \sim 113 \text{ km s}^{-1}$, thus overlapping the Terzan 5 distribution. When considering different metallicity bins, the bulge population is distributed as follows: (i) 3% with $[\text{Fe}/\text{H}] < -0.5$ dex; (ii) 44% with $-0.5 < [\text{Fe}/\text{H}] < 0$ dex; (iii) 49% with $0 < [\text{Fe}/\text{H}] < 0.5$ dex; (iv) 4% with $[\text{Fe}/\text{H}] > 0.5$ dex.

To perform a meaningful statistical decontamination we first split our sample in three radially selected sub-samples (see Fig. 6). The inner ($r < 100''$) subsample is composed of 66 stars. The fractions of field stars expected (Ferraro et al. 2014) to populate this inner region amounts to 2%, corresponding to a number of contaminating targets of about $N_{1,field} = 2$. The intermediate subsample ($100'' < r < 200''$) is composed of 48 stars. In this case, the number of expected field stars increases to $N_{2,field} = 16$, i.e. the 32% of the subsample. Finally, in the outer sample ($200'' < r < 276''$), where we count 21 stars, the expected contamination by non-member stars amounts to 73% (corresponding to $N_{3,field} = 16$). Fig. 6 summarizes the number of stars observed (in black) and the number of contaminants expected (in grey, encircled) in each radial and metallicity bin considered.

For each radially selected sub-sample and metallicity bin, we then randomly subtracted the corresponding number of expected contaminants, thus obtaining the decontaminated sample.

5.3. Decontaminated distribution

The final decontaminated sample is composed of 101 stars and its metallicity distribution is shown in the upper panel of Fig. 7. For comparison, the lower panel shows the distribution of the 34 giant stars in the innermost region ($r < 22''$) of Terzan 5 analyzed in O11 and the three metal-poor stars studied in O13. The two main peaks at sub-solar and super-solar metallicity, as well as the peak of the minor (5%) metal-poor component at $[\text{Fe}/\text{H}] \sim -0.8$ dex nicely match each other in the two distributions.

It is worth noticing that, while in the O11 sample the super-solar component is about as numerous as the sub-solar one (40% and 60%, respectively), in the FLAMES+DEIMOS distribution the component at ~ -0.3 dex is dominant. This essentially reflects the different radial distributions of the two stellar populations observed in Terzan 5, with the metal-rich stars being more concentrated (at $r < 20''$), and rapidly vanishing at $r \gtrsim 50''$ (see F09 and Lanzoni et al. 2010). Note, in fact, that while the 34 RGB stars observed by O11 are located at $r < 22''$, almost all the FLAMES+DEIMOS targets are at larger radial distances. In the FLAMES+DEIMOS distribution there are also three stars with very high metallicities ($[\text{Fe}/\text{H}] > +0.7$ dex). Given the small number of objects, at the moment we conservatively do not consider it as an additional sub-population of Terzan 5.

The overall metallicity distribution of Terzan 5, derived from a total of 135 stars (corresponding to 101 targets from the decontaminated FLAMES+DEIMOS sample discussed here, plus 34 NIRSPEC giants from O11) is shown in Fig. 8. In order to statistically verify the apparent multi-modal behavior of the distribution, we used the Gaussian mixture modeling (GMM) algorithm proposed by Muratov & Gnedin (2010). This algorithm determines whether a distribution is better described by a unimodal or a bimodal Gaussian fit. In particular, three requirements are needed to rule out the unimodality of a distribution:

1. the separation D between the peaks, normalized to the widths of the Gaussians, defined as in Ashman et al. (1994), has to be strictly larger than 2;
2. the kurtosis of the distribution has to be negative;
3. the likelihood ratio test (Wolfe 1971), which obeys χ^2 statistics, has to give sufficiently large values of χ^2 .

The algorithm also performs a parametric bootstrap to determine the confidence level at which the unimodality hypothesis can be accepted or rejected.

First of all, we computed the GMM test on the two main components. In this case, all the three requirements are verified ($D = 3.96$, kurtosis = -0.89 and $\chi^2 = 43.46$ with 4 degrees

of freedom) and the unimodal fit is rejected with a probability $P > 99.9\%$. We then repeated the same procedure considering the most metal-poor component at $[\text{Fe}/\text{H}] \simeq -0.8$ and the sub-solar one. Also in this case the unimodal fit is rejected with a probability $P > 99.9\%$ ⁶. We can therefore conclude that the metallicity distribution of Terzan 5 is clearly *multi-peaked*. We are able to reproduce its shape using three Gaussian profiles (red line in Fig. 8). Adopting the mean values and dispersions obtained from the GMM test, the two main peaks are located at $[\text{Fe}/\text{H}] \simeq -0.27$ dex (with $\sigma = 0.12$) and $[\text{Fe}/\text{H}] \simeq +0.25$ dex (with $\sigma = 0.12$), the sub-solar component being largely dominant (62% of the total). A minor component (6% of the total) is located at $[\text{Fe}/\text{H}] \simeq -0.77$ dex (with $\sigma = 0.11$).

Finally in Fig. 9 we show the radial distribution of the 135 stars (101 from this study and 34 from O11) adopted to construct the Terzan 5 metallicity distribution shown in Fig. 8: the multi-modal metallicity distribution is clearly evident also in this plot. It is worth of noticing that the most metal poor component is essentially located in the innermost 80'' from the cluster center, further supporting the membership of this minor component.

6. DISCUSSION AND CONCLUSIONS

The results presented in this work are based on a statistically significant sample of stars distributed over the entire radial extent of Terzan 5, thus solidly sampling the metallicity distribution of this stellar system. We confirm the previous claims by F09, O11 and O13 that Terzan 5 hosts multiple stellar populations characterized by significantly different iron contents.

The multi-modal iron distribution of Terzan 5 puts this stellar system in a completely different framework with respect to that of genuine GCs. In fact, the latter systems, although showing significant spreads in the abundance of light elements (as sodium, oxygen, aluminum etc.; see, e.g., Carretta et al. 2010a)⁷, still maintain a striking homogeneity in terms of iron content, thus indicating that their stellar populations formed within a potential well which was unable to retain the high-velocity gas ejected by violent SN explosions. Indeed, the

⁶ Note that because of the large difference in size between the two components, the computed kurtosis turns out to be positive. However we checked that by reducing the size of the sample belonging to the sub-solar component, the kurtosis turns negative, as required by the GMM test.

⁷This suggests that GC formation has been more complex than previously thought, having re-processed the low-energy ejecta from asymptotic giant branch stars (Ventura et al. 2001) and/or fast rotating massive stars (Decressin et al. 2007), with enrichment timescales of $\sim 10^8$ years or shorter (e.g., D’Ercole et al. 2008; Valcarce & Catelan 2011).

iron content of stellar populations can be considered the main feature to distinguish between genuine GCs and more complex stellar systems (Willman & Strader 2012). Following this view, Terzan 5 certainly belongs to the latter class of objects.

Recent high-precision spectroscopic studies have shown some iron spread (but still with a range largely smaller than 1 dex) in a few GCs, namely M22 (Marino et al. 2009, 2011a, 2012), M2 (Yong et al. 2014), and M54 (Carretta et al. 2010b)⁸. However, the iron distributions observed in these systems are unimodal, with no evidence of multiple peaks, as we also verified by means of the GMM test described above. Only M54 shows a tail towards the metal-rich side of its metallicity distribution, but this population can be severely contaminated by the Sagittarius field stars (see Bellazzini et al. 1999, 2008).

Only another GC-like system in the Galaxy (ω Centauri) is known to host a large variety of stellar sub-populations (Lee et al. 1999; Pancino et al. 2000; Ferraro et al. 2004, 2006; Bellini et al. 2009, 2010, 2013) with a large range of iron abundance ($\Delta[\text{Fe}/\text{H}] > 1$ dex; Norris & Da Costa 1995; Origlia et al. 2003; Sollima et al. 2004, 2007; Johnson & Pilachowski 2010; Villanova et al. 2014), similar to what is observed in Terzan 5. As shown in Figure 10, a few similarities between Terzan 5 and ω Centauri can be indeed recognized: *(i)* a broad extension of the iron distribution (~ 1.8 dex in Terzan 5 and ~ 2 dex in ω Centauri; see Johnson & Pilachowski 2010 for the latter); *(ii)* a multi-modal distribution; *(iii)* the presence of a numerically small stellar population ($\sim 5 - 10\%$ of the total in both cases) which is more metal-poor than the main peak, possibly corresponding to the first generation of stars in the system (see Pancino et al. 2011 for ω Centauri). The intrinsic large dispersion in $[\text{Fe}/\text{H}]$ indicates that in the past these systems were massive enough to retain the high-energy, high-velocity ejecta of SNe, allowing for multiple bursts of star formation from increasingly iron-enriched gas over timescales of the order of a few 10^9 years.

ω Centauri is now believed to be the remnant of a dwarf galaxy accreted by the Milky Way (e.g., Bekki & Freeman 2003). In contrast, the high metallicity regime of Terzan 5 (not observed in the known satellites of our Galaxy) and its tight chemical link with the Galactic bulge (O11, O13, M14a) make very unlikely that it has been accreted from outside the

⁸Other two GCs have been proposed to harbor intrinsic iron dispersion, namely NGC 5824 (Saviane et al. 2012; Da Costa et al. 2014) and NGC 3201 (Simmerer et al. 2013). We exclude these two clusters from our discussion because their intrinsic iron scatter has been not firmly confirmed. The analysis of NGC 5824 is based on the Calcium II triplet as a proxy of metallicity and direct measurements of iron lines from high-resolution spectra are not available yet. Moreover, based on HST photometry, Sanna et al. (2014) have recently found that the color distribution of RGB stars is consistent with no metallicity spread. Concerning NGC 3201, the analysis of Simmerer et al. (2013) leads to an appreciable iron spread among the stars of this cluster, but the analysis of Munoz, Geisler & Villanova (2013) contradicts this result.

Milky Way, and favor an in-situ formation. Terzan 5 could be the remnant of an early giant structure which may plausibly have contributed to form the Galactic bulge. In principle, the low dispersion of the iron content within each sub-population of Terzan 5 could be consistent with both a bursty star formation and chemical self-enrichment, and the dry merging of individual sub-structures with different metallicity (e.g. Immeli et al. 2004; Elmegreen et al. 2008; Förster Schreiber et al. 2011). However, the fact that among the three distinct sub-populations, the metal-rich one is more centrally concentrated than the more metal-poor ones seems to favor a self-enrichment scenario, at least for the formation of the metal-rich component (e.g. D’Ercole et al. 2008).

Certainly Terzan 5 is very peculiar, if not unique, system within the Galactic bulge. In order to solve the puzzle of its true nature, some pieces of information are still missing, such as the accurate estimate of the absolute ages of its populations, and a proper characterization of the global kinematical properties of the system.

We thank the anonymous referee for his/her useful comments and suggestions which helped us to improve the presentation of our results. This research is part of the project COSMIC-LAB (web site: <http://www.cosmic-lab.eu>) funded by the European Research Council (under contract ERC-2010-AdG-267675). M.B. acknowledges financial support from PRIN MIUR 2010-2011 project The Chemical and Dynamical Evolution of the Milky Way and Local Group Galaxies, prot. 2010LY5N2T. R. M. R. acknowledges support from US National Science Foundation grant AST-1212095 and from grant GO-12933 from the Space Telescope Science Institute. Some of the data presented herein were obtained at the W.M. Keck Observatory, which is operated as a scientific partnership among the California Institute of Technology, the University of California and the National Aeronautics and Space Administration. The Observatory was made possible by the generous financial support of the W.M. Keck Foundation. The authors wish to recognize and acknowledge the very significant cultural role and reverence that the summit of Mauna Kea has always had within the indigenous Hawaiian community. We are most fortunate to have the opportunity to conduct observations from this mountain.

REFERENCES

- Ashman, K. M., Bird, C. M., & Zepf, S. E. 1994, *AJ*, 108, 2348
- Bekki, K., & Freeman, K. C. 2003, *MNRAS*, 346, L11
- Bellazzini, M., Ferraro, F. R., & Buonanno, R. 1999, *MNRAS*, 307, 619

- Bellazzini, M., Ibata, R. A., Chapman, S. C., et al. 2008, *AJ*, 136, 1147
- Bellini, A., Piotto, G., Bedin, L. R., et al. 2009, *A&A*, 507, 1393
- Bellini, A., Bedin, L. R., Piotto, G., et al. 2010, *AJ*, 140, 631
- Bellini, A., Anderson, J., Salaris, M., et al. 2013, *ApJ*, 769, L32
- Carretta, E., Bragaglia, A., Gratton, R., et al. 2010, *ApJ*, 712, L21
- Carretta, E., Bragaglia, A., Gratton, R. G., et al. 2010, *ApJ*, 714, L7
- Castelli, F., & Kurucz, R. L. 2004, arXiv:astro-ph/0405087
- Da Costa, G. S., Held, E. V., & Saviane, I. 2014, *MNRAS*, 438, 3507
- Decressin, T., Charbonnel, C., & Meynet, G. 2007, *A&A*, 475, 859
- D’Ercole, A., Vesperini, E., D’Antona, F., McMillan, S. L. W., & Recchi, S. 2008, *MNRAS*, 391, 825
- Dotter, A., Chaboyer, B., Jevremović, D., Baron, E., Ferguson, J.-W., Sarajedini, A. & Anderson, J., 2007, *AJ*, 134, 376
- Elmegreen, B. G., Bournaud, F., & Elmegreen, D. M. 2008, *ApJ*, 688, 67
- Faber, S. et al., 2003, *SPIE*, 4841, 1657
- Ferraro, F. R., Sollima, A., Pancino, E., et al. 2004, *ApJ*, 603, L81
- Ferraro, F. R., Sollima, A., Rood, R. T., et al. 2006, *ApJ*, 638, 433
- Ferraro, F. R., Dalessandro, E., Mucciarelli, A., et al. 2009, *Nature*, 462, 483 (F09)
- Förster Schreiber, N. M., Shapley, A. E., Genzel, R., et al. 2011, *ApJ*, 739, 45
- Fulbright, J. P., McWilliam, A., & Rich, R. M. 2007, *ApJ*, 661, 1152
- Gustafsson, B., Edvardsson, B., Eriksson, K., Jorgensen, U. G., Nordlund, A. & Plez, B., 2008, *A&A*, 486, 951
- Hill, V., Lecureur, A., Gómez, A., et al. 2011, *A&A*, 534, A80
- Ibata, R., Sollima, A., Nipoti, C., Bellazzini, M., Chapman, S. C., & Dalessandro, E., 2011, *ApJ*, 738, 186

- Immeli, A., Samland, M., Gerhard, O., & Westera, P. 2004, *A&A*, 413, 547
- Johnson, C. I., & Pilachowski, C. A. 2010, *ApJ*, 722, 1373
- Johnson, C. I., Rich, R. M., Fulbright, J. P., Valenti, E., & McWilliam, A. 2011, *ApJ*, 732, 108
- Johnson, C. I., Rich, R. M., Kobayashi, C., & Fulbright, J. P. 2012, *ApJ*, 749, 175
- Johnson, C. I., Rich, R. M., Kobayashi, C., et al. 2013, *ApJ*, 765, 157
- Johnson, C. I., Rich, R. M., Kobayashi, C., Kunder, A., & Koch, A. 2014, arXiv:1407.2282
- Lanzoni, B., Ferraro, F. R., Dalessandro, E., et al. 2010, *ApJ*, 717, 653
- Lee, Y.-W., Joo, J.-M., Sohn, Y.-J., et al. 1999, *Nature*, 402, 55
- Marigo, P., Girardi, L., Bressan, A., Groenewegen, M. A. T., Silva, L., & Granato, G. L., 2008, *A&A*, 482, 883
- Marino, A. F., Milone, A. P., Piotto, G., et al. 2009, *A&A*, 505, 1099
- Marino, A. F. et al., 2011, *A&A*, 532, 8
- Marino, A. F. et al., 2012, *A&A*, 541, 15
- Massari, D., Mucciarelli, A., Dalessandro, E., et al. 2012, *ApJ*, 755, L32
- Massari, D., Mucciarelli, A., Ferraro, F. R., et al. 2014, *ApJ*, 791, 101 (M14a)
- McLean, I. S., Becklin, E. E., Bendiksen, O., et al. 1998, *Proc. SPIE*, 3354, 566
- Meszaros, Sz., Allende Prieto, C., Edvardsson, B., Castelli, F., Garcia Perez, A. E., Gustafsson, B., Majewski, S. R., Plez, B., Schiavon, R., Shetrone, M., & de Vicente, A., 2012, *AJ*, 144, 120
- Miocchi, P., Lanzoni, B., Ferraro, F. R., et al. 2013, *ApJ*, 774, 151
- Montegriffo, P., Ferraro, F. R., Origlia, L. & Fusi Pecci, F., 1998, *MNRAS*, 297, 872
- Mucciarelli, A., 2011, *A&A*, 528, 44
- Mucciarelli, A., Bellazzini, M., Ibata, R., Merle, T., Chapman, S. C., Dalessandro, E., & Sollima, A., 2012, *MNRAS*, 426, 2889
- Mucciarelli, A., Pancino, E., Lovisi, L., Ferraro, F. R., & Lapenna, E. 2013, *ApJ*, 766, 78

- Mucciarelli, A. 2013, arXiv:1311.1403
- Munoz, C., Geisler, D., & Villanova, S., 2013, MNRAS, 433, 2006
- Muratov, A. L., & Gnedin, O. Y. 2010, ApJ, 718, 1266
- Ness, M., Freeman, K., Athanassoula, E., et al. 2013, MNRAS, 430, 836
- Norris, J. E., & Da Costa, G. S. 1995, ApJ, 447, 680
- Origlia, L., Ferraro, F. R., Fusi Pecci, F., & Oliva, E. 1997, A&A, 321, 859
- Origlia, L., Ferraro, F. R., Bellazzini, M., & Pancino, E. 2003, ApJ, 591, 916
- Origlia, L., Rich, R. M., Ferraro, F. R., et al. 2011, ApJ, 726, L20 (O11)
- Origlia, L., Massari, D., Rich, R. M., et al. 2013, ApJ, 799, L5 (O13)
- Pancino, E., Ferraro, F. R., Bellazzini, M., Piotto, G., & Zoccali, M. 2000, ApJ, 534, L83
- Pancino, E., Mucciarelli, A., Sbordone, L., et al. 2011, A&A, 527, 18
- Pasquini, L., Avila, G., Blecha, A., et al. 2002, The Messenger, 110, 1
- Pietrinferni, A., Cassisi, S., Salaris, M., & Castelli, F. 2004, ApJ, 612, 168
- Pietrinferni, A., Cassisi, S., Salaris, M., & Castelli, F. 2006, ApJ, 642, 797
- Rich, R. M., Origlia, L., & Valenti, E. 2012, ApJ, 746, 59
- Sanna, N., Dalessandro, E., Ferraro, F. R., et al. 2014, ApJ, 780, 90
- Saviane, I., da Costa, G. S., Held, E. V., Sommariva, V., Gullieuszik, M., Barbuy, B., & Ortolani, S., 2012, A&A, 540, 27
- Sbordone, L., Bonifacio, P., Castelli, F., & Kurucz, R. L., MSAIS, 5, 93
- Simmerer, J., Ivans, I. I., Filler, D., Francois, P., Charbonnel, C., Monier, R., & James, G., 2013, ApJ, 764, 7L
- Sollima, A., Ferraro, F. R., Origlia, L., Pancino, E., & Bellazzini, M. 2004, A&A, 420, 173
- Sollima, A., Ferraro, F. R., Bellazzini, M., et al. 2007, ApJ, 654, 915
- Stetson, P. B., & Pancino, E. 2008, PASP, 120, 1332
- Valcarce, A. A. R., & Catelan, M. 2011, A&A, 533, A120

- Valenti, E., Ferraro, F. R., & Origlia, L. 2007, *AJ*, 133, 1287
- Valenti, E., Ferraro, F. R., & Origlia, L. 2010, *MNRAS*, 402, 1729
- Ventura, P., D’Antona, F., Mazzitelli, I., & Gratton, R. 2001, *ApJ*, 550, L65
- Villanova, S., Geisler, D., Gratton, R. G., & Cassisi, S. 2014, arXiv:1406.5069
- Yong, D., Roederer, I. U., Grundahl, F., et al. 2014, *MNRAS*, 441, 3396
- Willman, B., & Strader, J., 2012, *AJ*, 144, 76
- Wolfe, A. M. 1971, *BAAS*, 3, 474
- Zoccali, M., Hill, V., Lecureur, A., et al. 2008, *A&A*, 486, 177

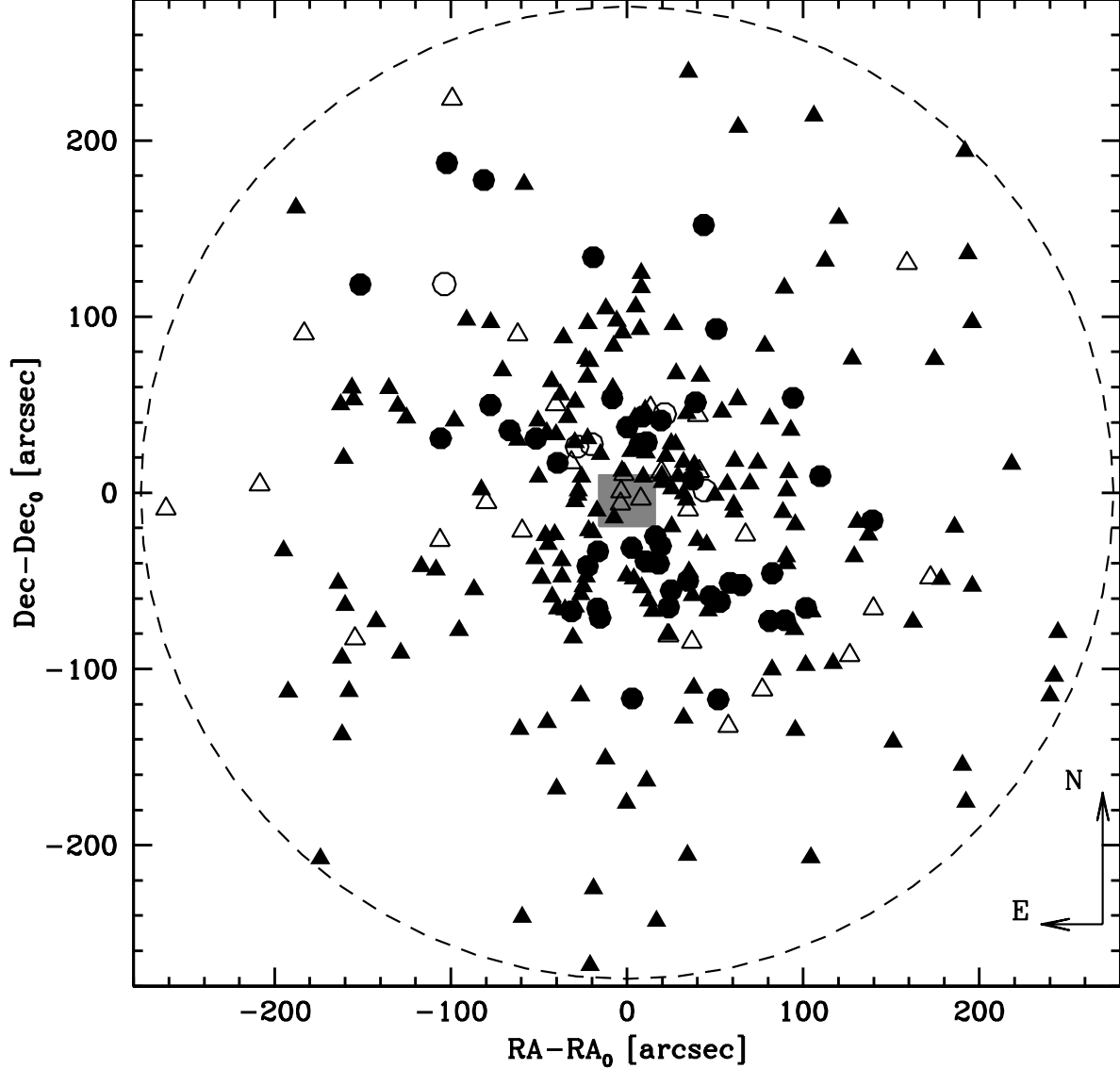


Fig. 1.— Spatial distribution of the spectroscopic targets in Terzan 5. FLAMES and DEIMOS targets are shown as triangles and circles, respectively. The central gray square marks the region where the NIRSPEC targets are located (see Section 5.1 for the details about the membership). Filled symbols mark targets for which the iron abundance was measured while empty symbols are used to indicate targets affected by TiO contamination for which no abundance determination was possible. The dashed circle marks the tidal radius of the system, $r_t = 276'' = 7.9$ pc ($100''$ corresponding to 2.86 pc at the distance of Terzan 5).

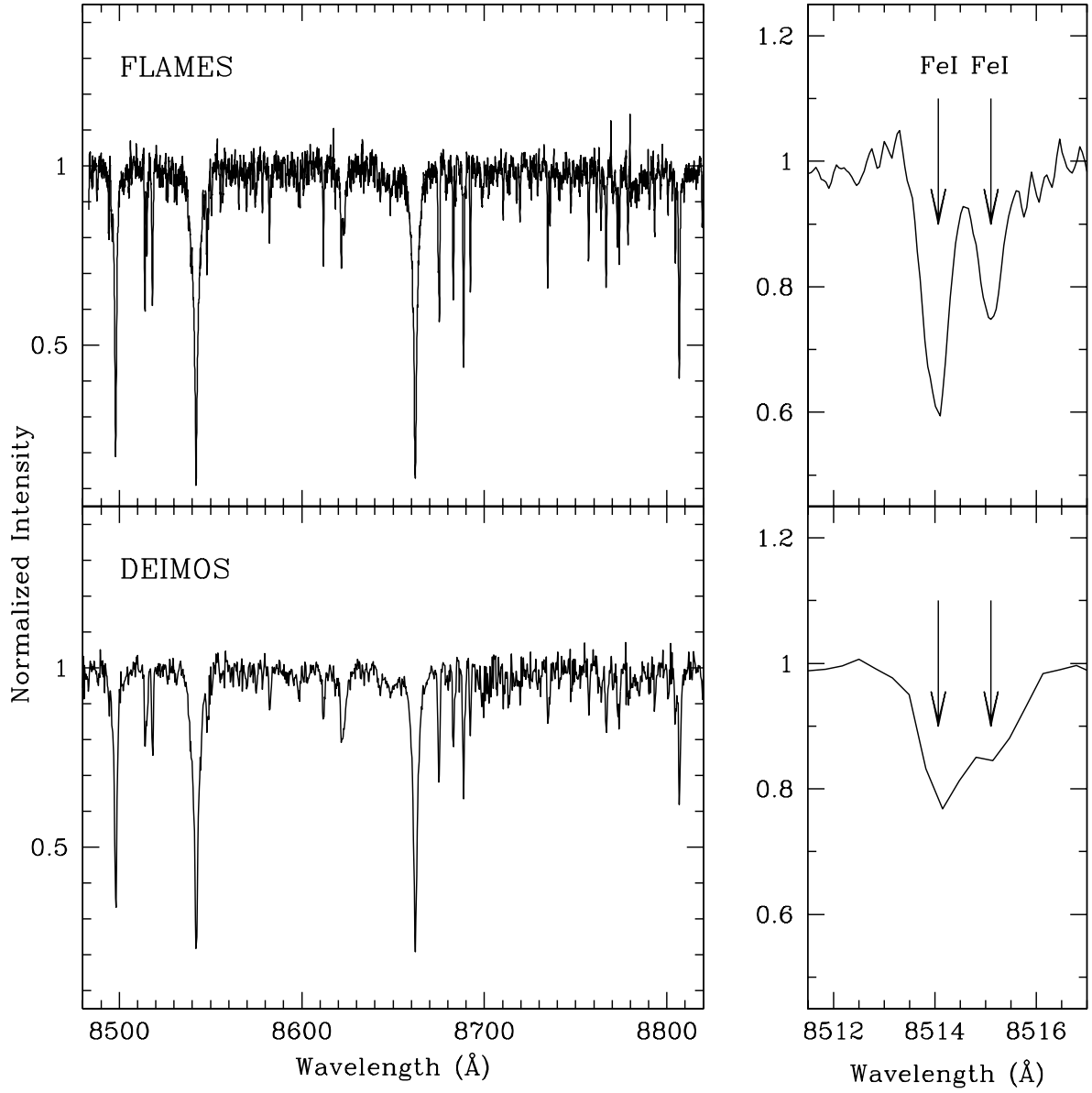


Fig. 2.— The Ca II triplet spectral region for star 34, as obtained from FLAMES (left-upper panel) and DEIMOS (left-lower panel) observations. The right panels show the zoomed spectra around two Fe I lines used in the analysis.

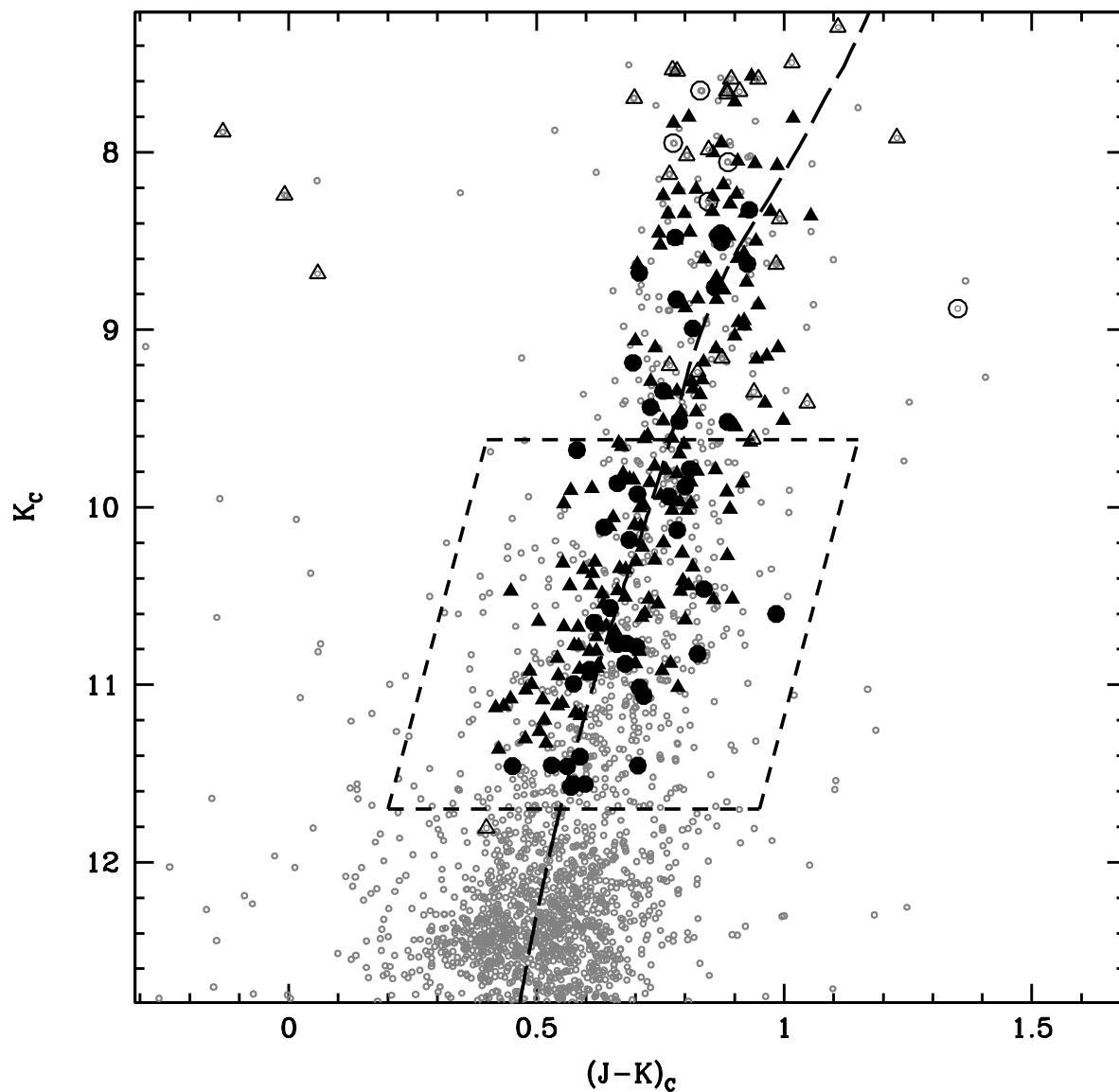


Fig. 3.— Infrared CMD of Terzan 5 corrected for differential reddening. Symbols are as in Fig. 1, with empty symbols marking the targets affected by TiO contamination. The BaSTI isochrone with an age of 12 Gyr and metallicity $Z=0.01$ used to derive the atmospheric parameters is also shown as a long-dashed line. The box delimited by the short-dashed line indicates the sample not affected by TiO contamination that was selected to compute the metallicity distribution.

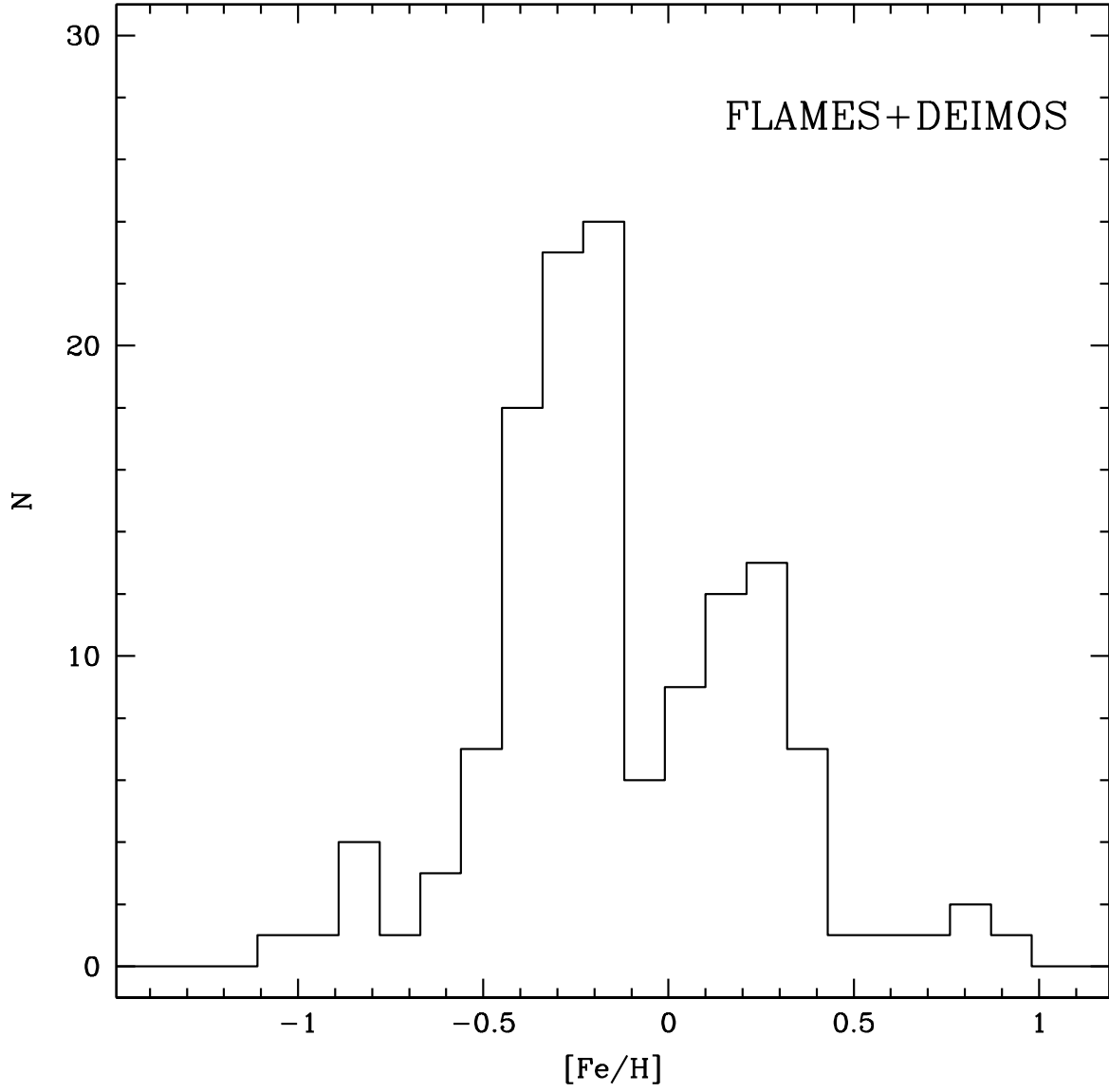


Fig. 4.— Metallicity distribution obtained for the unbiased FLAMES+DEIMOS sample (135 targets selected in the magnitude range $9.6 < K_c < 11.7$), before the statistical decontamination.

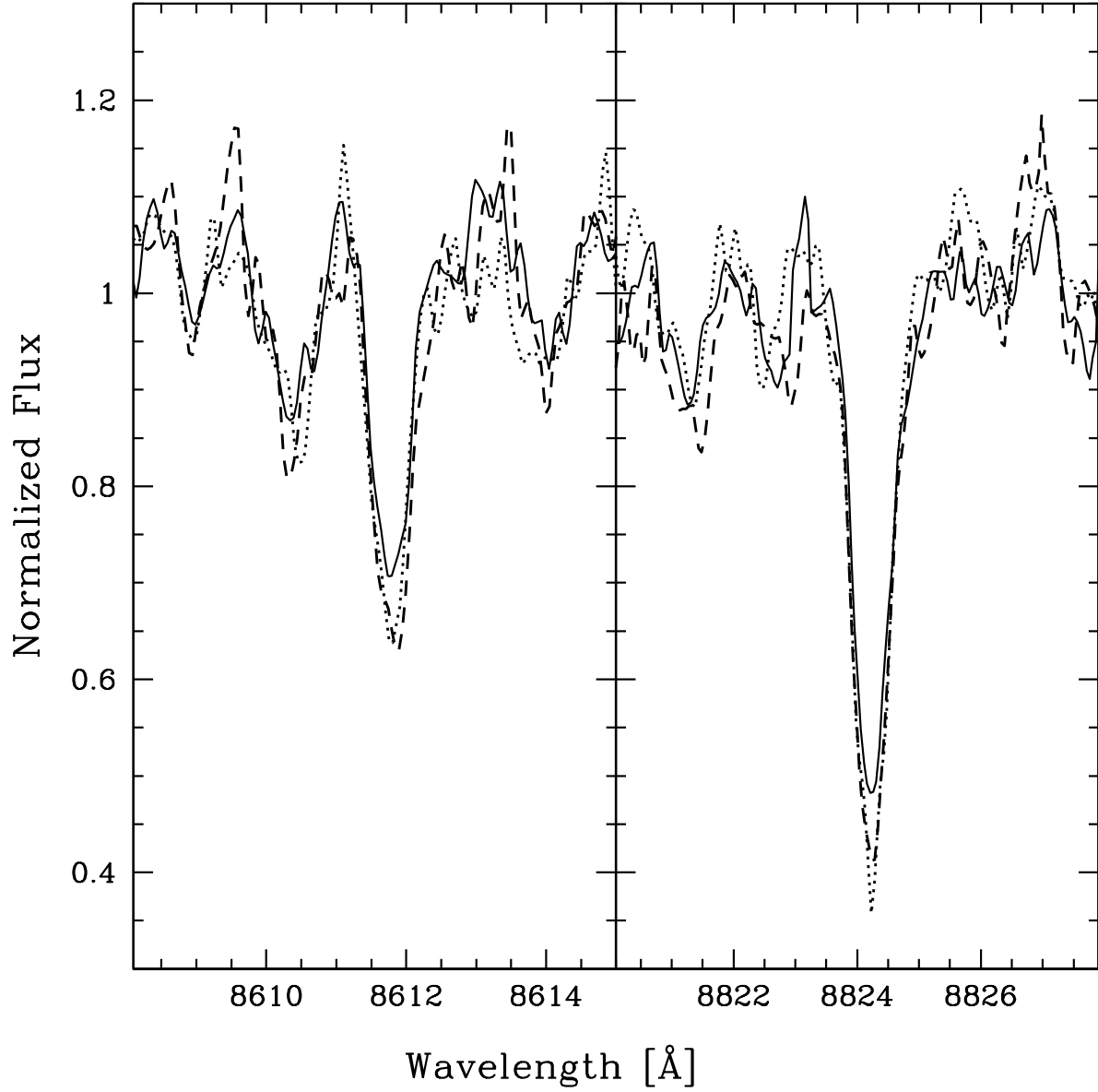


Fig. 5.— Comparison of the spectra of two super metal-rich stars (namely 7009197 and 7036045, shown as dashed and dotted line, respectively) and that of a star at $[\text{Fe}/\text{H}] = +0.26$ (solid line) with similar atmospheric parameters. The two super metal-rich stars show more pronounced absorption lines, thus indicating an actual, very high metallicity.

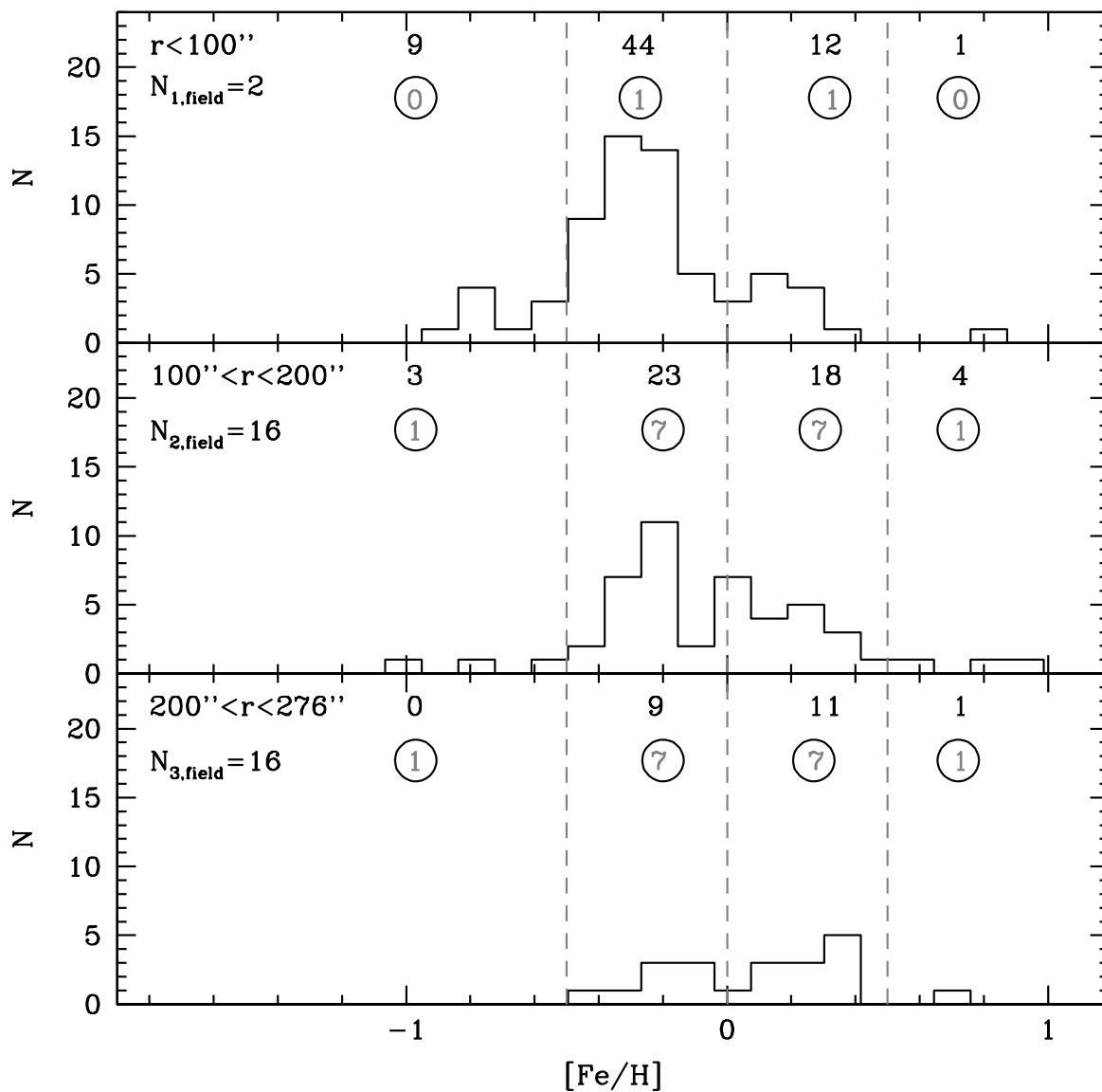


Fig. 6.— Metallicity distributions of Terzan 5 stars in the inner $r < 100''$ (*upper panel*), intermediate $100'' < r < 200''$ (*middle panel*) and outer $170'' < r < 276''$ (*lower panel*) annuli. The total number of expected contaminants in each radial bin is reported in the upper-left corner of each panel. The number of stars observed in each metallicity bin (delimited by vertical dashed lines) is quoted, while the number of contaminants to be statistically subtracted is highlighted in grey and encircled in black.

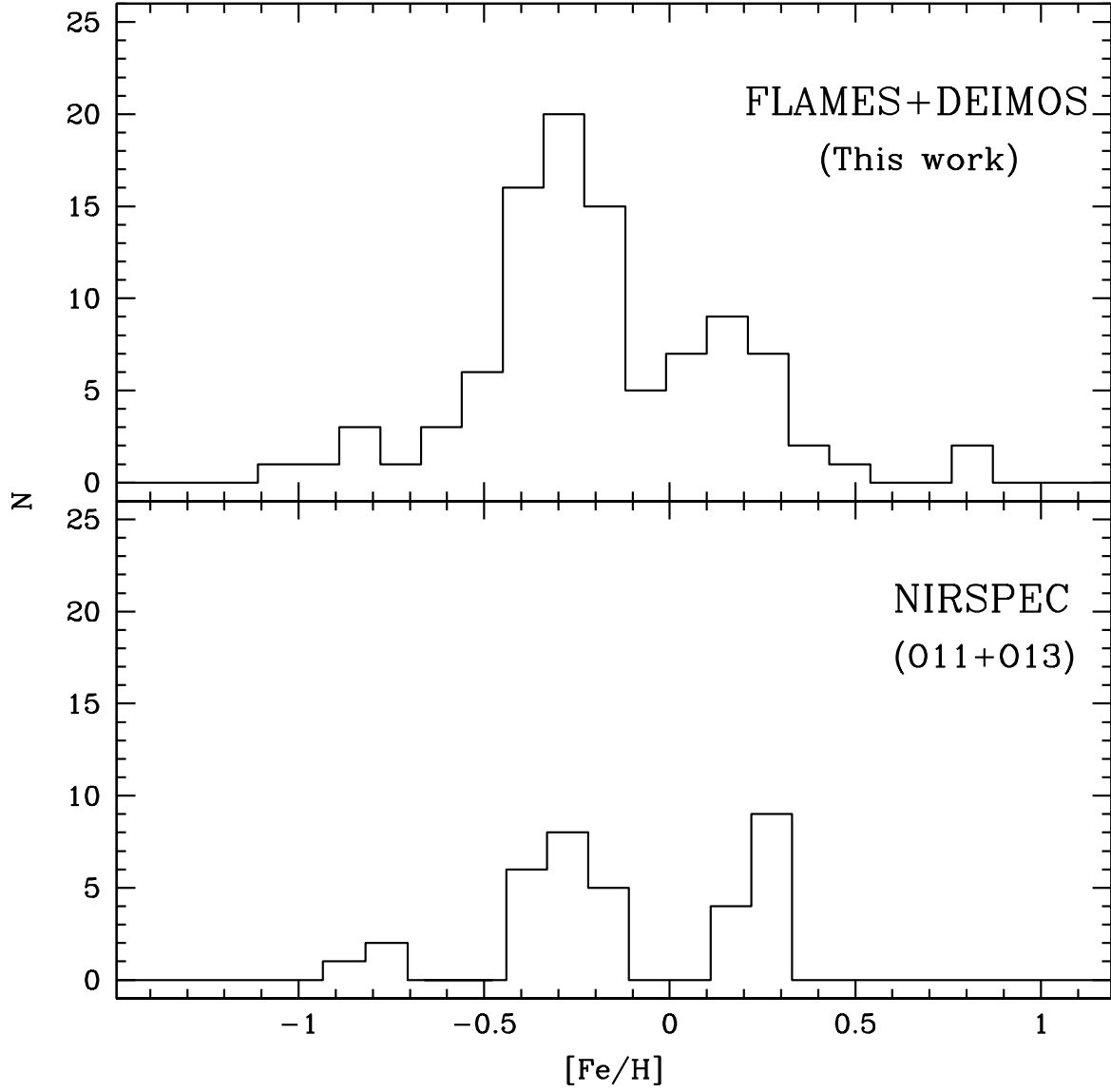


Fig. 7.— Statistically decontaminated metallicity distribution for the FLAMES+DEIMOS sample (101 stars, upper panel), compared to that derived by O11 and O13 (34 and 3 stars respectively, lower panel).

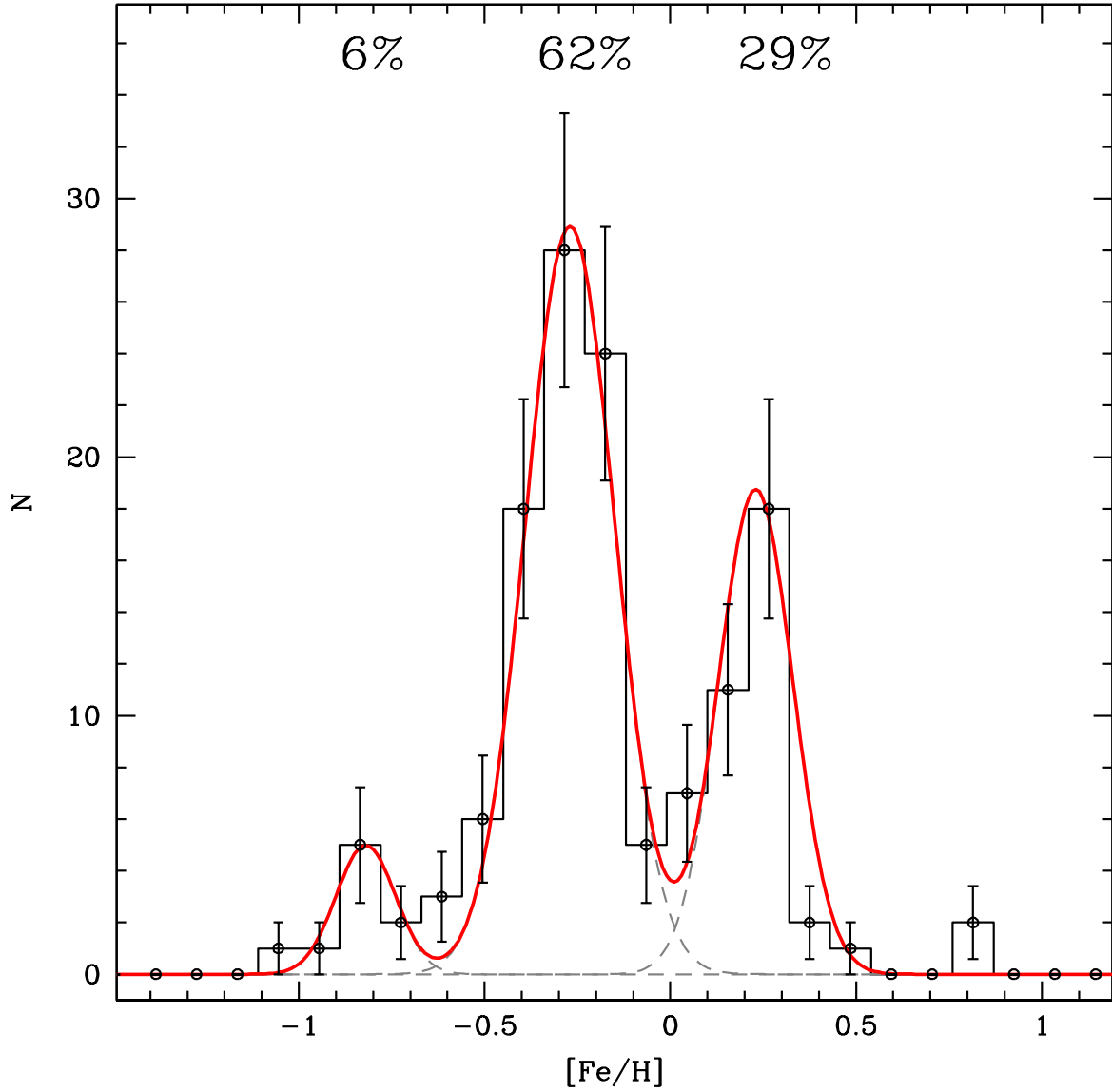


Fig. 8.— Decontaminated metallicity distribution for the combined FLAMES+DEIMOS (101 stars, this work) and NIRSPEC (34 targets, O11) spectroscopic samples. The solid red line shows the fit that best reproduces the observed distribution using three Gaussian profiles. Individual Gaussian components are shown as grey dashed lines. The percentage of each individual component with respect to the total sample of 135 stars is also reported.

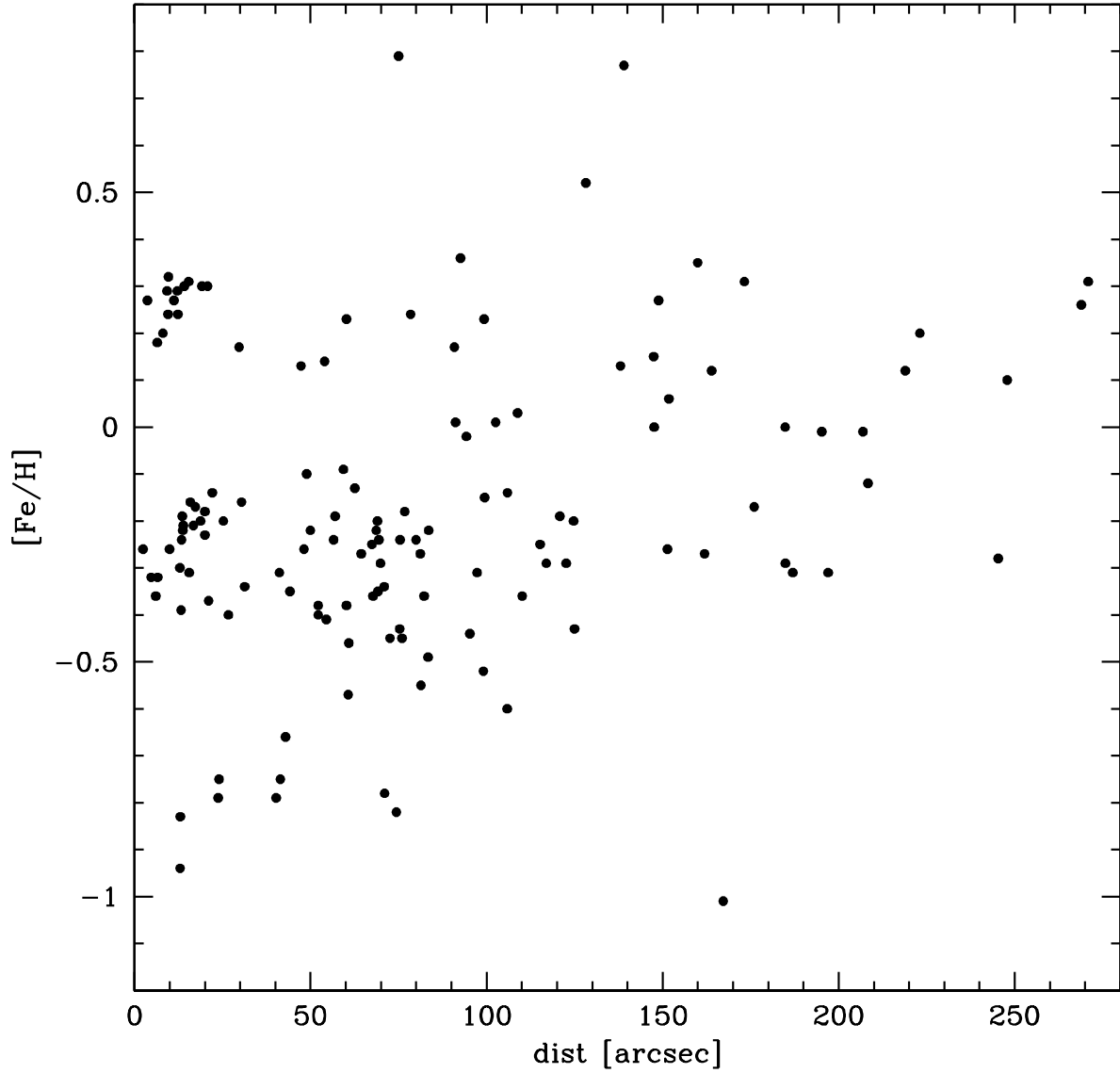


Fig. 9.— The $[Fe/H]$ distribution as a function of the distance from the cluster center for the 135 stars composing the final decontaminated iron distribution shown in Fig 8: the multi-modality of the metallicity distribution is clearly evident. The bulk of each of the three components is located in the innermost $80''$ from the cluster center, thus further confirming the actual membership of all the three populations.

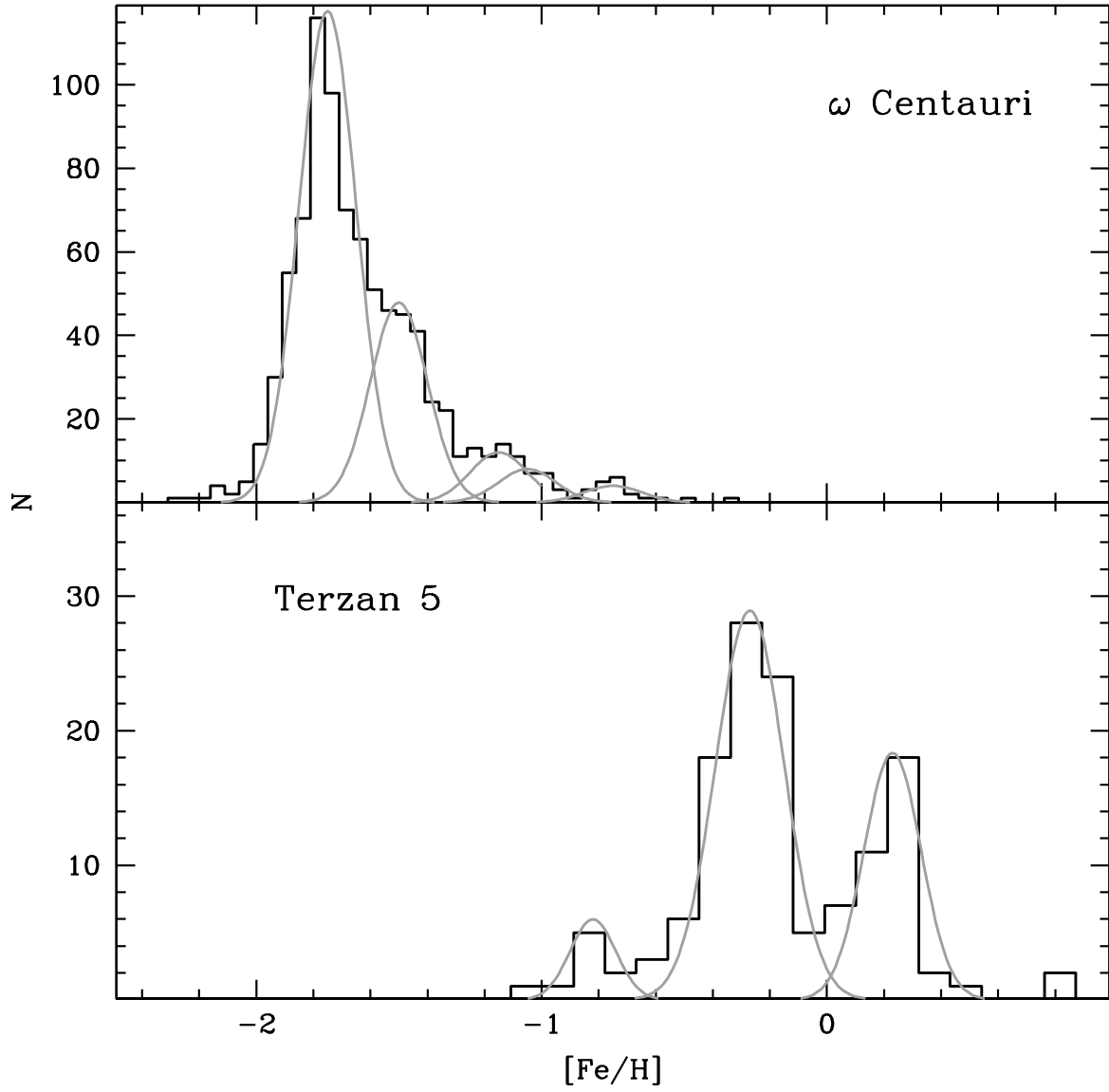


Fig. 10.— The metallicity distribution of ω Centauri (*upper panel*) and Terzan 5 (*lower panel*). The distribution of ω Centauri, together with the five Gaussians reproducing its multi-modality, have been taken from Johnson & Pilachowski (2010).

Table 1. Iron abundance of Terzan 5 stars.

ID	RA	Dec	K_c (mag)	T_{eff} (K)	$\log g$ (cm s^{-2})	[Fe/H] (dex)	$\sigma_{[\text{Fe}/\text{H}]}$ (dex)	Dataset
109	266.9801977	-24.7835577	8.60	3741	0.7	-0.30	0.17	FLAMES
126	267.0292394	-24.7803417	8.60	3736	0.7	-0.26	0.14	FLAMES
134	267.0332227	-24.7953548	8.73	3771	0.7	-0.32	0.07	FLAMES
146	267.0254477	-24.7817867	8.78	3786	0.8	-0.38	0.07	FLAMES
148	267.0291700	-24.7969272	8.86	3804	0.8	-0.17	0.06	FLAMES
155	267.0286940	-24.7786346	8.83	3799	0.8	-0.34	0.09	FLAMES
158	267.0124475	-24.7843182	8.88	3814	0.8	-0.36	0.10	FLAMES
159	267.0226507	-24.7624999	8.83	3800	0.8	-0.32	0.06	FLAMES
164	267.0282685	-24.7949808	8.98	3838	0.8	-0.31	0.07	FLAMES
165	267.0315361	-24.7896355	8.95	3831	0.8	-0.18	0.15	FLAMES

Note. — Identification number, coordinates, K_c magnitude atmospheric parameters, iron abundances and their uncertainties, and corresponding dataset for all the 220 stars members of Terzan 5 with iron abundance measured. All stars with $K_c < 9.6$ or $K_c > 11.7$ have been excluded from the analysis of the MDF (see Section 5.1).